RSC Advances

PAPER

View Article Online
View Journal | View Issue

Cite this: *RSC Adv.*, 2024, **14**, 17491

A dual-signal optical sensing platform of CDs–MnO_2 NS composites for facile detection of ascorbic acid based on a combination of Tyndall effect scattering and fluorescence†

ShuJing Zhou,[a] Jing Wan,[a] Jianmei Zou,[*a] Yulan Zhang,[a] Huijun He,[b] Wei Li,[a] Jiale Hu,[a] Jinfang Nie,[a] Yali Yuan[a] and Yun Zhang[*a]

A dual-signal optical sensing platform was successfully developed for the determination of ascorbic acid (AA) based on blue fluorescent carbon dots (CDs) and manganese dioxide nanosheets (MnO_2 NSs) with strong Tyndall effect (TE) scattering and fluorescence quenching capabilities. In this nanosystem, CDs–MnO_2 NS composites were employed as probes to evaluate the AA concentration. Owing to the strong reduction, the presence of the target AA could reduce the MnO_2 NSs to Mn^{2+} and induce the degradation of the MnO_2 NSs, resulting in a significant decrease in the TE scattering intensity of the MnO_2 NSs and the fluorescence recovery of the CDs. Therefore, a novel optical sensor based on TE scattering and fluorescence dual detectors was developed for the sensitive determination of AA. Under optimized conditions, the limits of detection (LODs) of the two modes were 113 and 3 nM, respectively. Furthermore, the dual-signal optical sensing platform was successfully applied for the detection of AA in human serum.

Received 27th March 2024
Accepted 16th May 2024

DOI: 10.1039/d4ra02340d

rsc.li/rsc-advances

1. Introduction

Ascorbic acid (AA), a crucial water-soluble vitamin in the human body, plays an essential role in maintaining normal metabolism.[1] Owing to its strong reducing ability, AA exhibits excellent antioxidant effects and can effectively scavenge free radicals to maintain cellular redox metabolism homeostasis.[2,3] As a neuromodulator, AA plays an important role in promoting the synthesis of neurotransmitters and facilitating the differentiation, maturation, and survival of neurons.[4,5] In addition, AA is an important cofactor for various enzymes that assist in the biosynthesis of collagen, tyrosine metabolism, and activation of peptide hormones.[6] For human health, the required daily dose of AA is 100 mg. Because the human body cannot synthesize AA endogenously, it is necessary to acquire adequate AA from the diet.[7] Previous studies have shown that abnormal AA levels in the human body can induce several diseases such as scurvy, bleeding, diabetes mellitus, cancer, urinary stones, gastrospasms, neurodegenerative diseases, and psychiatric disorders.[8–10] Thus, it is important to establish a rapid, sensitive, accurate, and convenient method for monitoring AA levels for clinical disease diagnosis.

A series of new methods have been developed for AA determination, including liquid chromatography,[11] electrochemistry,[12–14] electrochemiluminescence,[15] chromatography,[16] fluorescence,[17,18] and colorimetry.[19–21] Because of their distinct merits of low cost, simple operation, and easy access to equipment, fluorescence and colorimetric methods have been widely applied to analyze AA in real samples.[22] However, most of these methods suffer from large background signal interference and environmental fluctuations owing to their single-signal detectors. In practice, a sensing platform capable of providing a dual-signal detector will be more appropriate for the highly accurate and sensitive detection of AA.

Recently, manganese dioxide nanosheets (MnO_2 NSs), a type of two-dimensional redox-active layered transition-metal dioxide nanomaterial, have drawn significant attention in various fields owing to their large specific surface area, excellent biocompatibility, robust physicochemical properties, strong oxidizing properties, unique optical properties, ease of modification, and low cytotoxicity.[23,24] In sensing platforms, MnO_2 NSs usually serve as recognition elements,[25] nanoenzymes,[26] or fluorescence quenchers.[27] On the one hand, since the valence state of Mn^{4+} in MnO_2 NSs is the intermediate valence, MnO_2 NSs possess strong oxidation capacity and catalytic activity.[28] Thus, MnO_2 NSs can react with reducing substances (such as AA and GSH) and cause their decomposition, making them reliable recognition units for reducing substances in biosensing. In addition, because of their

[a]College of Chemistry and Bioengineering, Guilin University of Technology, Guilin 541004, P. R. China. E-mail: 2019136@glut.edu.cn; zy@glut.edu.cn; Fax: +86 773 5896839; Tel: +86 773 5896453

[b]Guangxi Key Laboratory of Environmental Pollution Control Theory and Technology, Guilin University of Technology, Guilin 541004, China

† Electronic supplementary information (ESI) available. See DOI: https://doi.org/10.1039/d4ra02340d

strong oxidation ability, MnO_2 NSs are ideal nanoenzymes that can catalyze the oxidation of various organic compounds, resulting in the discoloration of substrate dyes, which can be used for the construction of colorimetric sensing platforms.[29–31] On the other hand, owing to their intense and broad absorption spectrum, MnO_2 NSs can effectively quench the fluorescence of organic dyes/fluorescent nanomaterials through Förster resonance energy transfer (FRET) and the inner filter effect (IFE), which makes them often act as efficient fluorescence quenchers in various biosensing nano-platforms.[32–34]

In the above methods, the degraded or nondegraded state of MnO_2 NSs can lead to changes in their oxidation ability and absorption spectra, which is the basis for the signal transduction of these nanomaterial sensing platforms.[35,36] Moreover, when the particle size is changed, the scattering optical phenomena of MnO_2 NSs is also affected. Several previous reports have shown that sensing methods based on the Tyndall effect (TE, an interesting visible light scattering phenomenon commonly occurring in colloidal solutions) of other nanomaterials provide more sensitive qualitative and quantitative analytical performance in terms of sensitivity, portability, and cost.[37] However, to the best of our knowledge, the TE of MnO_2 NSs has not been discussed in the field of sensing. Furthermore, the vast majority of current TE-based sensing strategies only use a single-signal detector, whereas dual-signal sensors that provide two independent output modes and improve detection accuracy are rarely explored. As mentioned above, the MnO_2 NSs in different states exhibited different TE signals and absorption spectra. The TE signals of MnO_2 NSs in different dispersed states can be used as quantitative data for colorimetric systems. Meanwhile, their different absorption can be combined with luminescent donors and converted into fluorescent signals. Carbon dots (CDs), which are environmentally friendly fluorescent nanomaterials with excellent optical properties, exhibit great potential for the fabrication of fluorescent sensors for multiple detection.[38]

In this study, a TE scattering and fluorescence dual-signal optical sensing platform based on CDs–MnO_2 NS composites was successfully constructed for the detection of AA. The dual-signal optical probe was formed by mixing MnO_2 NSs and CDs, and the design principle of this sensor is shown in Fig. 1. In this system, MnO_2 NSs act as AA recognition units, TE signal transducers, and fluorescence quenchers. On the one hand, because of their large dimensions, the MnO_2 NSs provide a strong red TE signal under the illumination of a handheld 635 nm laser pointer pen. One the other hand, because of their intense and broad absorption spectra, the MnO_2 NSs can efficiently quench the fluorescence of CDs *via* FRET. In the presence of the analyte AA, the MnO_2 NSs were reduced to Mn^{2+}, and their structures were degraded into smaller nanoparticles, resulting in a significant reduction in the TE signal of the MnO_2 NSs and the fluorescence recovery of the CDs. Based on this principle, a highly sensitive and accurate dual-signal optical sensing platform was established for AA detection and was successfully applied to the analysis of AA levels in human serum. To the best of our knowledge, this is the first example of the application of the TE of MnO_2 NSs to construct a dual-signal sensing platform.

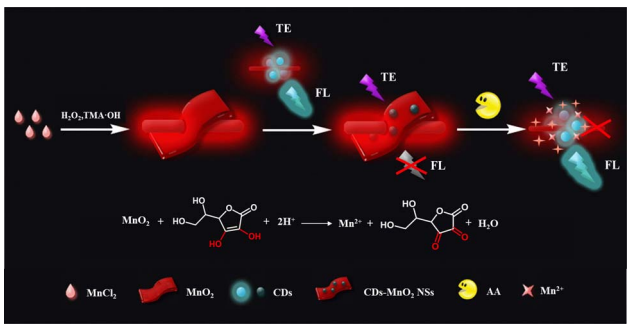

Fig. 1 Schematic of the TE scattering and fluorescence dual-signal optical sensing platform based on the CDs–MnO_2 NS composites for AA detection.

2. Experimental section

2.1. Materials and apparatus

Manganese chloride ($MnCl_2$), tetramethylammonium hydroxide (TMA·OH), ammonium bicarbonate (NH_4HCO_3), sodium citrate ($C_6H_5O_7Na_3$), urea, L-arginine (L-Arg), L-lysine (L-Lys), L-leucine (L-Leu), L-proline (L-Pro), L-tryptophan (L-Trp), L-serine (L-Ser), L-threonine (L-Thr), L-valine (L-Val), L-histidine (L-His), fructose (Fru), glucose (Glu), $FeCl_3 \cdot 6H_2O$, $CoCl_2 \cdot 6H_2O$, $CuCl_2 \cdot 2H_2O$, $Zn(NO_3)_3$, and $MgCl_2 \cdot 6H_2O$ were purchased from Aladin Chemical Reagent Co., Ltd (Shanghai, China). Methanol (CH_3OH) was obtained from Fuyu Fine Chemical Co., Ltd (Tianjin, China). Hydrogen peroxide (H_2O_2) was purchased from Chengdu Colon Chemical Co., Ltd. All other chemicals were of analytical grade and were used as received without further purification. Serum samples were obtained from a university hospital. Unless stated otherwise, all stock solutions were prepared with deionized water (with a specific resistivity ≥18.2 MΩ cm) that was produced by an ultrapure water system (UPS-II-20L) from Chengdu Yuechun Technology Co., Ltd (Chengdu, China).

Fluorescence was measured using an F-7000 fluorescence spectrophotometer (Hitachi, Tokyo, Japan). Optical characterization of the MnO_2 NSs was performed using a UV-vis spectrometer (Cary 50, Varian, USA). X-ray photoelectron spectroscopy (XPS) of CDs was performed on a Kratos AXIS HSI spectrometer to characterize their composition. The morphology characterization were performed using transmission electron microscopy (TEM, JEM-2100F, JEOL, Japan). Hydrated particle size and the zeta potential of MnO_2 NSs and CDs was measured using the Zetasizer Nano ZS90 instrument (Malvern Instruments Ltd, Britain). TE signals were produced using a 635 nm red laser pointer pen (5 mW; handheld light source) purchased from Deli Group Co., Ltd (Ningbo, China). All colorimetric images were recorded using a smartphone (Xiaomi 6A) and analyzed using ImageJ.

2.2. Preparation of MnO_2 NSs and CDs

MnO_2 NSs were prepared according to a previously reported method with slight modifications.[39] Briefly, 2.1748 g of

TMA·OH was dissolved in 3% of 20 mL H_2O_2 and was quickly injected into 10 mL of $MnCl_2$ (0.3775 g) with vigorous stirring. The resulting suspension was then stirred overnight at room temperature. The product was washed three times with a mixture of methanol and ultrapure water and collected by centrifugation at 8000 rpm for 10 min. Subsequently, the resulting MnO_2 NSs were freeze–dried. To prepare the MnO_2 NSs solution, 20 mg of freeze–dried MnO_2 NSs powder was dissolved in 20 mL of water and sonicated for 5 h. The mixture was centrifuged at 5000 rpm for 5 min, and the supernatant was collected and stored in a refrigerator until further use.

The synthesis of CDs refers to a simple hydrothermal method with some modification.[40] In detail, 0.3 g of sodium citrate and 2.25 g of ammonium bicarbonate were dissolved in 10 mL of water to obtain a clear solution. The mixture was transferred into a 50 mL polytetrafluoroethylene autoclave and reacted at 180 °C for 4 h. After cooling to ambient temperature, the solution was transferred to a dialysis membrane (3000 Da, molecular weight cutoff) and dialyzed for approximately 48 h with a water exchange every 2 h. The obtained CDs were stored at 4 °C for further use.

2.3. Dual-mode detection of AA

Briefly, 100 μL of MnO_2 NSs (40 μg mL^{-1}) and 100 μL of CDs solution were first mixed in 750 μL of PB buffer (10 mM, pH 7). Subsequently, 50 μL of AA solutions with different concentrations were added into the mixture solution and reacted at 25 °C for 30 min. The resulting solution was then used for the quantitative analysis of AA through dual optical channels. The fluorescence intensity of the resulting solution was measured at an excitation wavelength of 354 nm. For the TE signaling method, the resulting solution was illuminated with a portable red laser pointer pen, and the TE images of all the samples were captured using a smartphone. ImageJ processing software was used to analyze the average gray (AG) value of each TE image as the TE intensity. TE-based quantities were calculated according to: $\Delta AG = AG_{blank} - AG_{sample}$, where AG_{blank} and AG_{sample} were obtained from the CDs–MnO_2 NS solution treated without or with AA sample, respectively. Selectivity tests were performed in the same manner by detecting D-Glu, L-Ala, L-Arg, L-Lys, L-Leu, L-Pro, L-Trp, L-Ser, L-Thr, L-Val, L-His, K^+, Mg^{2+}, Na^+, Fru, urea, Glu, Lac, and sucrose instead of AA.

2.4. Determination of AA in human serum samples

To investigate the performance of the as-prepared CDs–MnO_2 NS platform in real samples, it was used to detect the concentration of AA in clinical serum samples. Clinical whole blood samples were acquired from the Guilin University of Technology Hospital (Guilin, China). Before detection, clinical whole blood samples were filtered through a 0.45 mm microporous membrane to obtain human serum. All the pretreated samples were then diluted with buffer to meet the linear detection range. The obtained solution was used as a practical stock solution of AA for fluorescence and TE detection, following the processes described in the previous section.

3. Results and discussion

3.1. Characterization of synthesized CDs, MnO_2 NSs and CDs–MnO_2 NS composites

To successfully construct a dual-signal optical sensor combining fluorescence and TE signals, small-sized CDs with excellent fluorescence properties and large-sized MnO_2 NSs with good light absorption properties were prepared. As shown in Fig. 2A, the TEM image shows that the prepared-MnO_2 NSs exhibited a typical wrinkle and fold-large-sized nanosheet morphology, which is similar to that in previous literature.[41] The large nanostructure of the MnO_2 NSs makes them reliable materials for TE-based sensors. In addition, the UV-vis absorption spectrum of the MnO_2 NSs exhibited a wide characteristic absorption in the range of 200–800 nm with a maximum peak at 361 nm (Fig. S1†), which is a typical curve for MnO_2 NSs according to a previous report, making them excellent fluorescence quenchers.[42]

In this study, CDs were synthesized by a one-step hydrothermal method, and their morphology and size were characterized by TEM and dynamic light scattering (DLS). As shown in Fig. 2B, the as-prepared CDs were nearly monodispersed in a spherical shape with a narrow size distribution of approximately 9.1 nm (inset of Fig. 2B). In addition, the optical properties of the CDs were characterized using UV-vis absorption and fluorescence spectroscopy. As shown in Fig. 2C, the CDs exhibited a moderate absorption peak at 331 nm and a single narrow emission peak at 445 nm upon excitation at 354 nm. The CD solution was colorless under visible light and emitted a bright blue fluorescence under UV light (inset of Fig. 2C). Moreover, the fluorescence emission of the CDs showed excitation-independent characteristics, and the emission peak

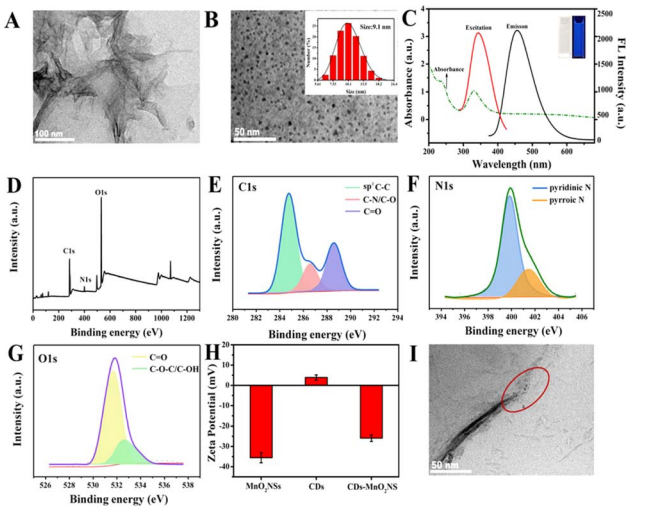

Fig. 2 (A) TEM images of MnO_2 NSs. (B) TEM images of CDs. Inset shows the size distribution of CDs. (C) UV-vis absorption spectra of CDs and excitation and emission fluorescence spectra of CDs. Inset shows CDs under sunlight and ultraviolet light. (D) XPS survey spectrum of CDs. (E) C 1s, (F) N 1s, and (G) O 1s high-resolution XPS profiles of CDs. (H) Zeta potential of CDs, MnO_2 NSs, and CDs-MnO_2 NS. (I) TEM images of CDs–MnO_2 NS composites.

at 445 nm did not shift in the excitation range from 280 to 400 nm, which could be attributed to the narrow size distribution of the CDs (Fig. S2†). In addition, the surface chemical states and elemental compositions of the CDs were investigated using XPS. As shown in Fig. 2D, the results indicated that the CDs were mainly composed of C, N, and O with the corresponding contents of 55.75%, 3.95%, and 40.3%, respectively. The C 1s high-resolution XPS spectrum was fitted to three peaks centered at 284.8, 286.6, and 288.6 eV, attributing to SP^2–C–C, C–N/C–O, and C═O, respectively (Fig. 2E). The N 1s XPS spectrum exhibited peaks corresponding to pyridinic N (399.8 eV) and pyrrolic N (401.5 eV) (Fig. 2F), whereas O 1s exhibited peaks corresponding to C═O (531.7 eV) and C–O–C/C–OH (532.6 eV) (Fig. 2G).

After successfully synthesizing the CD and MnO_2 NSs, the formation of the CDs–MnO_2 NS composite was further verified. As illustrated in Fig. 2H, the zeta potentials of MnO_2 NSs and CDs alone were −34.05 and 4.63 mV, respectively, while the potential of the CDs–MnO_2 NS nanocomposites was −24.47 mV. These results demonstrate the existence of strong electrostatic interactions between the two nanomaterials, which could result in the formation of new complexes or keep them close to each other. Moreover, TEM images (Fig. 2I) show that the small CDs were successfully attached to the surface of the MnO_2 NSs, indicating the successful formation of CDs–MnO_2 NS composites.

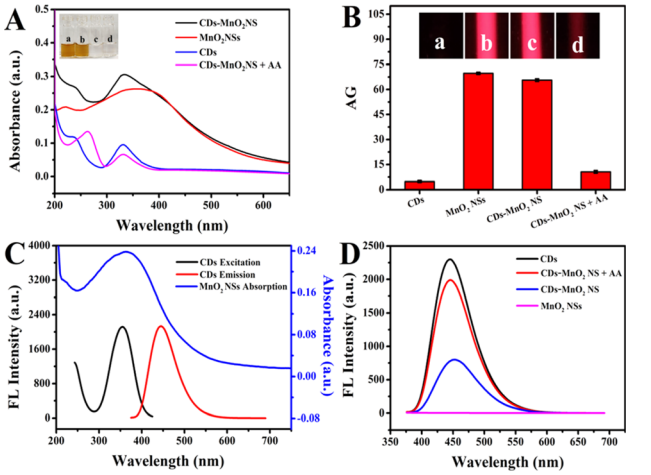

Fig. 3 (A) UV-vis absorption spectra of different samples: CDs–MnO_2 NS, MnO_2 NSs, CDs and CDs–MnO_2 NS + AA. Inset shows the corresponding photograph of different samples: (a) CDs–MnO_2 NS, (b) MnO_2 NSs, (c) CDs and (d) CDs–MnO_2 NS + AA. (B) The corresponding average grayscale (AG) results of the TE images shown in inset. Inset shows TE results obtained from different samples: (a) CDs, (b) MnO_2 NSs, (c) CDs–MnO_2 NS, (d) CDs–MnO_2 NS + AA. (C) UV-vis absorption spectra of MnO_2 NSs and excitation and emission fluorescence spectra of CDs. (D) Fluorescence emission spectra from 375 to 700 nm of CDs (black line), CDs–MnO_2 NS + AA(red line), CDs–MnO_2 NS (blue line) and MnO_2 NSs (magenta line) at excitation wavelength of 354 nm.

3.2. Feasibility of AA detection based on the CDs–MnO_2 NS dual-signal optical sensing platform

The design strategy for the dual-signal optical assay is shown in Fig. 1. In this system, MnO_2 NSs could not only serve as recognition units for AA but also as signal transducers of TE and fluorescence quenchers. Because of the strong reducibility of the target AA, the MnO_2 NSs were reduced to Mn^{2+} and decomposed in the presence of AA, resulting in a significant decrease in the TE signal of the MnO_2 NSs and the release of the fluorescent probe CDs. Consequently, the dual-signal determination of AA was achieved. After the successful construction of the CDs–MnO_2 NS complex, the feasibility of the AA-induced degradation of the MnO_2 NSs was investigated. As shown in Fig. 3A, the freshly prepared CDs–MnO_2 NS solution appeared yellowish-brown, similar to the color of the MnO_2 NS solution (inset of Fig. 3A). When the target AA was added to the CDs–MnO_2 NS solution, the yellowish-brown color faded, and the absorption intensity of the MnO_2 NSs sharply decreased in the UV-vis spectrum, whereas the change in the absorption intensity of the CDs at 331 nm was negligible. Moreover, the FT-IR spectra showed that the peak located at 515 cm^{-1} could be attributed to the Mn–O stretching vibration of MnO_2 NSs (Fig. S3†). As for the CDs, the obvious peak at 1640 cm^{-1} can be assigned to the asymmetric stretching vibration of the carboxylate anion, which comes from the precursor of sodium citrate. The high intensity peak at 3460 cm^{-1} corresponds to the stretching vibration of –OH. When CDs were adsorbed on the MnO_2 NSs, the FT-IR spectrum of CDs–MnO_2 NS complex contained both the characteristic peaks of CDs (1640 cm^{-1}, and 3460 cm^{-1} for the carboxylate anion and –OH) and the MnO_2 NSs (515 cm^{-1} for Mn–O bonds). However, when AA was added into the CDs–MnO_2 NS solution, the peak of Mn–O stretching vibration disappears. All of the above results imply that the addition of AA-induced the degradation of MnO_2 NSs but not CDs. Importantly, because of the larger size of the MnO_2 NSs in the probe, they showed a strong TE signal under irradiation by a 635 nm red laser pointer (Fig. 3B). However, the CDs are small, their TE signals can be ignored in the system. Therefore, the degradation of the MnO_2 NSs by the addition of AA significantly decreased the TE signals of the system, and a notable decrease in the average gray (AG) values was observed. The above results indicate the feasibility of the AA-adjusted TE signals of the CDs–MnO_2 NS system.

Subsequently, the fluorescence detection of AA based on the CDs–MnO_2 NS system was verified. As shown in Fig. 3C, the maximum excitation and emission peaks of the CDs were nearly completely within the absorption spectrum of the MnO_2 NSs, indicating that the MnO_2 NSs may be ideal quenchers for quenching CD fluorescence. As shown in Fig. 3D, in the absence of the target AA, the fluorescence of the CDs was effectively quenched by MnO_2 NSs (blue lines). In the presence of the target AA, as proved in Fig. 3A, the MnO_2 NSs were reduced to Mn^{2+} and degraded, which enabled the release of CDs and caused distinct fluorescence recovery in this system (red lines). It was suggested that the fluorescence signal change based on the CDs–MnO_2 NS system could be used to detect AA. In addition, a possible mechanism by which the MnO_2 NSs quench CD fluorescence was explored. As proven in our previous experimental results, the superior light absorption capability of the

MnO_2 NSs overlapped well with the emission spectrum and absorption peak of the CDs. Owing to the strong electrostatic interaction, a CDs–MnO_2 NS nanocomposite was constructed, which enabled the emission energy of CDs was transferred to the MnO_2 NSs in close vicinity. Furthermore, the fluorescence lifetime of CDs was reduced from 5.7 ns to 5.2 ns after mixing with MnO_2 NSs (Fig. S4†). All of the results indicated that the fluorescence of the CDs quenched by the MnO_2 NSs was a FRET process.

3.3. Optimization of experimental conditions

After confirming the feasibility of AA detection using this dual-signal optical platform, several experimental factors that may affect the dual-readout assay were optimized to achieve the best analytical performance for AA detection. Firstly, as recognition units, TE signal transducers, and fluorescence quenchers in this system, the concentration of MnO_2 NSs had a significant influence on the sensitivity of this system and was an important factor to be discussed. To optimize the experimental conditions of TE and fluorescence dual optical channels, the ΔAG ($\Delta AG = AG_{Blank} - AG_{Sample}$) and ΔFL ($\Delta FL = FL_{Sample} - FL_{Blank}$) were taken as standard, respectively. As shown in Fig. S5A and S6A,† the general trend of ΔAG and ΔFL was to increase with the increasing MnO_2 NSs concentration and all of them rose to the peak values at 40 μg mL^{-1}. Consequently, 40 μg mL^{-1} was selected as the optimal condition for further experiments.

Under this MnO_2 NSs concentration, the kinetic response of the dual-signal optical sensing system for AA detection was studied. After incubating AA with the CDs–MnO_2 NS system for different times (5, 10, 20, 30, 60, 90, 120, and 180 min), the TE and fluorescence signals of the mixtures were monitored in real-time. With the increase of reaction time from 5 to 30 min, the ΔAG and ΔFL gradually increased and reached their maximum values (Fig. S5B and S6B,† respectively). The results revealed that the CDs–MnO_2 NS nanocomposites completely reacted with AA in 30 min and exhibited the maximum signal change to achieve sensitive detection. Thus, 30 min was selected as the optimal reaction time for the subsequent experiments. In addition, the pH values and temperatures tested for this reaction were comprehensively investigated. The results showed that optimal detection conditions were obtained at pH 7.0 (Fig. S5C and S6C,† respectively) and the optimal reaction temperature was 25 °C (Fig. S5D and S6D,† respectively).

3.4. AA detection performance of the CDs–MnO_2 NS dual-signal optical sensing platform

Under the optimized reaction conditions, the AA detection performance of the CDs–MnO_2 NS dual-signal optical sensing platform was evaluated. For TE detection, as shown in Fig. 4A, the CDs–MnO_2 NS solution that was not treated with AA exhibited notable TE signals under the illumination of a hand-held red laser pointer. While the TE signal intensity of the system decreased gradually as the AA concentration increased from 0.4 to 400 μM, which could be attributed to the AA-induced MnO_2 NSs degradation. A quantitative analysis of these TE images was performed using ImageJ, and the corresponding

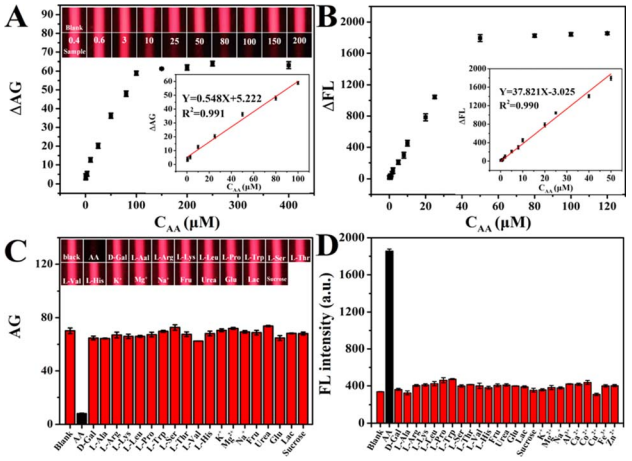

Fig. 4 (A) TE photos and ΔAG value recorded from the mixing of CD–MnO_2 NS and AA of different concentrations: 0.4, 0.6, 3, 10, 25, 50, 80, 100, 150, 200, 250 and 400 μM. Inset: linear plot of ΔAG value and AA concentration. (B) The change of fluorescence intensity recorded from the mixing of CD–MnO_2 NS and AA of different concentrations: 0.02, 0.05, 0.2, 0.6, 0.8, 1, 5, 2, 5, 8, 10, 20, 25, 40, 50, 80, 100, and 120 μM. Inset: linear plot of fluorescence intensity and AA concentration. (C) AG value and (D) fluorescence intensity obtained from the blank solution (without AA), sample solution with 50 μM AA, and other interference substances (500 μM).

calibration curve revealed that the ΔAG values were linearly proportional to the AA levels between 0.4 and 100 μM (R^2 = 0.991, inset of Fig. 4A) and the detection limit was ~113 nM obtained by the 3σ rule. The TE detection, as a new noninstrumental colorimetric method, can be completed using a laser pointer and smartphone. Moreover, compared to other colorimetric methods, TE detection provides a wider linear range and a lower detection limit (Table S1†).

For fluorescence detection, since AA-induced the degradation of the MnO_2 NSs in the CDs–MnO_2 NS system, the fluorescent units CDs were released from MnO_2 NSs, and the fluorescence intensity of CDs was gradually recovered when the AA concentration increased from 0 to 50 μM (Fig. 4B and S7†). The results showed a good linear calibration plot of the change in fluorescence intensity and AA concentration in the range of 0.02–50 μM ($R^2 = 0.990$) with a detection limit of ~3 nM (inset of Fig. 4B). Compared with numerous previously reported AA fluorescence analytical methods, the detection range and limit of our proposed strategy were wider and lower, respectively (Table S1†).

To evaluate the selectivity of the CDs–MnO_2 NS dual-signal optical sensing platform, a target AA sample (50 μM) and various possible interference substances (D-Glu, L-Ala, L-Arg, L-Lys, L-Leu, L-Pro, L-Trp, L-Ser, L-Thr, L-Val, L-His, K^+, Mg^{2+}, Na^+, Fru, urea, Glu, Lac, sucrose; 500 μM) were measured separately by this method under the same conditions. It could be observed from Fig. 4C that a weak TE signal intensity was achieved in the presence of AA, whereas similarly strong TE signal intensities were obtained from the blank solution and various interfering substances. Meanwhile, the fluorescence interference study revealed that even when the concentration of the interfering

Table 1 Recovery of AA in human serum samples detected by the dual-signal optical sensing platform

Sample	Foud[a] AA (μM)	Added (μM)	Total[b] (μM)	Recovery (%)	RSD[c] (n = 6, %)	Channel
1	2.55	0	2.76	—	2.64	TE
2		25	28.75	104.80	2.30	TE
3		50	52.49	99.88	2.96	TE
4		0	2.63	—	4.40	FL
5		5	7.37	96.40	3.17	FL
6		10	12.53	99.80	2.84	FL

[a] Foud, the concentration of AA was determined by high performance liquid chromatography. [b] Total, the concentration of AA determined by the TE – fluorescence dual signal sensor. [c] RSD, relative standard deviation.

compounds was 10 times higher than that of AA, they did not significantly affect the fluorescence intensity, and only AA was able to achieve recovered fluorescence (Fig. 4D). The results indicate that the CDs–MnO_2 NS dual-signal optical sensing platform possesses excellent selectivity toward AA and can be applied to actual sample analyses.

Finally, to further verify the accuracy and practicality of the dual-signal optical sensing platform, the AA concentration in human serum samples was determined and experiments on the recovery of AA in real samples were conducted. Before analysis, the human serum samples were filtered through a 0.45 μm filter to remove large suspended particles and were diluted appropriately with the PB buffer (10 mM, pH 7) to keep AA concentrations within the linear range of this platform. As listed in Table 1, the measured AA concentrations in the human serum samples detected by both methods were 2.76 and 2.63 μM, respectively, which was close to the result confirmed by high-performance liquid chromatography (HPLC). The recovery of AA in human serum ranged from 96.40% to 104.80%, in which the obtained relative standard deviations (RSDs) were between 2.30% to 4.40% (n = 6). Thus, the results demonstrate the relatively high accuracy and practicality of the dual-signal optical sensing platform for practical applications.

4. Conclusion

In summary, based on the TE scattering of MnO_2 NSs and FRET between CDs and MnO_2 NSs, a dual-signal optical sensing platform for the selective and sensitive detection of AA was successfully constructed. The addition of AA reduced the MnO_2 NSs to Mn^{2+}, leading to the fragmentation of the MnO_2 NSs, which caused the TE significantly decrease of MnO_2 NSs and the fluorescence recovery of the CDs. Thus, the AA concentration can be evaluated from the corresponding changes in the TE and fluorescence signals in this nanosystem. The linear ranges of this dual-signal optical sensing platform for AA detection were 0.4–100 and 0.02–50 μM, respectively. The LOD for the TE and fluorometric methods were 113 and 3 nM, respectively. Compared with other single-signal probes, the dual-signal sensor exhibited the advantages of a slight error and a wide detection range. Furthermore, this system was successfully used to detect AA content in real human serum, demonstrating that dual-signal optical sensing has potential applications in clinical testing. This study not only developed a novel strategy for analyzing AA but also applied more optical properties of MnO_2 NSs for chemical analysis.

Author contributions

J. M. Z. and S. J. Z. conceived the concept and experiments. S. J. Z. and J. W. carried out the materials synthesis, characterizations, data curation, writing – original draft, writing – review & editing. J. M. Z carried out the writing – review & editing, supervision, project administration and funding acquisition. H. H. J., Y. L. Z., W. L. and J. L. H. analyzed the results. J. M. Z, Y. L. Y., J. F. N. and Y. Z. co-wrote the paper and revised the paper. All authors discussed the results and commented on the manuscript.

Conflicts of interest

There are no conflicts to declare.

Acknowledgements

This research was supported by the Guangxi Science & Technology Planning Project (No. Guike-AD21220146), National Natural Science Foundation of China (No. 22264011), Scientific Research Staring Foundation of Guilin University of Technology (No. GUTQDJJ2019136).

References

1 X. Hou, G. Zhan, X. Huang, N. Wang, Z. Ai and L. Zhang, *Chem. Eng. J.*, 2019, **382**, 122355.
2 S. J. Devaki and R. L. Raveendran, *Vitamin C*, 2017, p. 70162.
3 M. C. M. Vissers and A. B. Das, *Front. Physiol.*, 2018, **9**, 809.
4 R. Figueroa-Méndez and S. Rivas-Arancibia, *Front. Physiol.*, 2016, **6**, 397.
5 J. M. May, Z.-C. Qu, R. Nazarewicz and S. Dikalov, *Brain Res. Bull.*, 2012, **90**, 35–42.
6 T. Dodevska, D. Hadzhiev and I. Shterev, *Micromachines*, 2022, **14**, 41.
7 A. C. Carr and B. Frei, *Am. J. Clin. Nutr.*, 1999, **69**, 1086–1107.
8 I. Crha, D. Hrubá, P. Ventruba, J. Fiala, J. Totusek and H. Visnová, *Cent. Eur. J. Publ. Health*, 2003, **11**, 63–67.

9 M. Moretti, D. B. Fraga and A. L. S. Rodrigues, *CNS Neurosci. Ther.*, 2017, **23**, 921–929.
10 M. Moretti, D. B. Fraga and A. L. S. Rodrigues, *CNS Drugs*, 2017, **31**, 571–583.
11 Z. Gazdik, O. Zitka, J. Petrlova, V. Adam, J. Zehnalek, A. Horna, V. Reznicek, M. Beklova and R. Kizek, *Sensors*, 2008, **8**, 7097–7112.
12 F. Yang, J. Wang, Y. Cao, L. Zhang and X. Zhang, *Sens. Actuators, B*, 2014, **205**, 20–25.
13 Q. Lian, Z. He, Q. He, A. Luo, K. Yan, D. Zhang, X. Lu and X. Zhou, *Anal. Chim. Acta*, 2014, **823**, 32–39.
14 A. Barberis, Y. Spissu, G. Bazzu, A. Fadda, E. Azara, D. Sanna, M. Schirra and P. A. Serra, *Anal. Chem.*, 2014, **86**, 8727–8734.
15 H. Wang, G. Pu, S. Devaramani, Y. Wang, Z. Yang, L. Li, X. Ma and X. Lu, *Anal. Chem.*, 2018, **90**, 4871–4877.
16 X. Li and A. A. Franke, *J. Chromatogr. B*, 2009, **877**, 853–856.
17 X. Luo, W. Zhang, Y. Han, X. Chen, L. Zhu, W. Tang, J. Wang, T. Yue and Z. Li, *Food Chem.*, 2018, **258**, 214–221.
18 F. Ma, J. Luo, X. Li, S. Liu, M. Yang and X. Chen, *Spectrochim. Acta, Part A*, 2020, **249**, 119343.
19 J. Wan, J.-M. Zou, S.-J. Zhou, F.-L. Pan, F. Hua, Y.-L. Zhang, J.-F. Nie and Y. Zhang, *Anal. Methods*, 2023, **15**, 1819–1825.
20 M. Chi, Y. Zhu, L. Jing, C. Wang and X. Lu, *Talanta*, 2018, **191**, 171–179.
21 Y. Ding, M. Zhao, J. Yu, Z. Li, X. Zhang, Y. Ma, H. Li and S. Chen, *Talanta*, 2020, **219**, 121299.
22 A. Wu, H. Ding, W. Zhang, H. Rao, L. Wang, Y. Chen, C. Lu and X. Wang, *Food Chem.*, 2021, **363**, 130325.
23 L. Huang, S. Qin, Y. Xu, S. Cheng, J. Yang and Y.-L. Wang, *Microchem. J.*, 2023, **190**, 108719.
24 Z. Qian, R. Tan, X. Zhang, Y. Leng and Z. Chen, *Microchem. J.*, 2022, **181**, 107758.
25 D. He, X. He, K. Wang, X. Yang, X. Yang, X. Li and Z. Zou, *Chem. Commun.*, 2014, **50**, 11049–11052.
26 X. Yan, Y. Song, X. Wu, C. Zhu, X. Su, D. Du and Y. Lin, *Nanoscale*, 2017, **9**, 2317–2323.
27 J. Li, Y. Weng, C. Shen, J. Luo, D. Yu and Z. Cao, *Anal. Methods*, 2021, **13**, 2981–2988.
28 Y. Deng, W. Tang, W. Li and Y. Chen, *Catal. Today*, 2017, **308**, 58–63.
29 Z. Qian, L. Yang, W. Wei, J. Huang, D. Lu, S. Liu and X. Shi, *Microchem. J.*, 2023, **190**, 108625.
30 H. Sun, K. Xu, M. Huang, Y. Shang, P. She, S. Yin and Z. Liu, *Appl. Surf. Sci.*, 2015, **357**, 69–73.
31 L. Han, P. Liu, H. Zhang, F. Li and A. Liu, *Chem. Commun.*, 2017, **53**, 5216–5219.
32 S. Haque, S. Tripathy and C. R. Patra, *Nanoscale*, 2021, **13**, 16405–16426.
33 D. H. Sharanabasava, B. Mainak and C. Amrita, *ACS Appl. Nano Mater.*, 2022, **5**, 17373–17412.
34 S. Lin, H. Cheng, Q. Ouyang and H. Wei, *Anal. Methods*, 2016, **8**, 3935–3940.
35 R. Qian, D. Gao, L. Liu and Y. Jiang, *Anal. Methods*, 2020, **13**, 769–775.
36 W. Huang, Y. Deng and Y. He, *Biosens. Bioelectron.*, 2016, **91**, 89–94.
37 J. Huang, X. Mo, H. Fu, Y. Sun, Q. Gao, X. Chen, J. Zou, Y. Yuan, J. Nie and Y. Zhang, *Sens. Actuators, B*, 2021, **344**, 130218.
38 Q. Tang, Y. Fan, L. Han, Y. Yang, N. Li and H. Luo, *Mikrochim. Acta*, 2020, **187**, 1–9.
39 J. Lin, G. Liu, Z. Qiu, L. Huang and S. Weng, *New J. Chem.*, 2022, **46**, 12836–12843.
40 X. Qin, Y. Lu, M. Bian, Z. Xiao, Y. Zhang and Y. Yuan, *Anal. Chim. Acta*, 2019, **1091**, 119–126.
41 Y. Lin, Q. Zhou, D. Tang, R. Niessner and D. Knopp, *Anal. Chem.*, 2017, **89**, 5637–5645.
42 H. Yu and L. Zheng, *Mikrochim. Acta*, 2016, **183**, 2229–2234.